




# Material response and failure of highly deformable carbon fiber composite shells

## Journal Article

**Author(s):**

Schlothauer, Arthur ; Pappas, Georgios A. ; Ermanni, Paolo 

**Publication date:**

2020-10-20

**Permanent link:**

<https://doi.org/10.3929/ethz-b-000430824>

**Rights / license:**

[Creative Commons Attribution 4.0 International](#)

**Originally published in:**

Composites Science and Technology 199, <https://doi.org/10.1016/j.compscitech.2020.108378>

**Funding acknowledgement:**

150729 - Optical measurement of three-dimensional surface displacement fields of morphing structures (SNF)



# Material response and failure of highly deformable carbon fiber composite shells

Arthur Schlothauer<sup>\*,1</sup>, Georgios A. Pappas<sup>1</sup>, Paolo Ermanni

Laboratory of Composite Materials and Adaptive Structures, ETH Zürich, Leonhardstrasse 21, 8092 Zürich, Switzerland

## ARTICLE INFO

### Keywords:

Carbon fiber A.  
Non-linear behavior B.  
Modeling C.  
Deformation C.  
Thin shell composites

## ABSTRACT

Very thin carbon fiber composite shells can withstand large bending curvatures without failure. The resulting high tensile and compressive strains require accurate modeling of the fiber-dominated non-linear effects to predict the mechanical response. To date, no universal modeling technique can precisely capture the behavior of such structures. In this work, successful representation of composite's response was achieved by utilizing single fiber tension and compression experimental data, implemented to extend a basal-plane-realignment based non-linear carbon fiber material model. Numerical techniques were adopted to model the bending behavior of unidirectional carbon fiber composites that was recorded in a comprehensive experimental campaign. Observations show that high material non-linearity leads to a non-negligible neutral-axis shift and drastic reduction of bending modulus due to compressive softening. Tensile fiber failure is the driving mechanism in thin shells flexure allowing for elastic compressive strains of up to 3% without micro-buckling. As a result, a remarkable flexibility in thin shells is realized. With increasing thickness, the elastic flexibility is reduced as the failure-driving mode switches to compressive micro-buckling.

## 1. Introduction

Thin, unidirectional (UD) carbon fiber (CF) composite shells can be folded to impressively small bending radii without failure [1]. The ability to elastically sustain and recover large deformations makes these materials highly beneficial for applications like deployable space structures [2], future medical devices [3] or shape adaptable metamaterials [4]. Non-linear structural response was observed in previous experimental investigations at high bending strains [5,6], an effect attributed to the non-linear constitutive behavior of the CF. The accurate prediction of the elastic response of these structures is of crucial importance, as it strongly influences folding forces, shape recovery and damage.

Although some analytical constitutive models for the non-linear single fiber behavior in tension exist [7–9], none of them could so far precisely capture large deformation bending load cases, which requires accurate representation of both tensile and compressive behavior over a large strain range. To date, this behavior could only be represented by semi-empirical formulations [6], which matched the global stiffness of the tested coupons. Moreover, the influence of the non-linear elastic material behavior on the unique failure mechanisms found in highly deformable shells is still under investigation. Overall, the lack of understanding and of modeling capabilities of such structures prevents efficient and reliable design.

This paper presents a comprehensive experimental and numerical approach to observe, understand and model highly deformable CF composites in the elastic regime. The approach included the measurement of underlying strain distribution and global response in thin shell composites subjected to large bending deformation until failure. Emphasis was laid on the accurate representation of the elastic behavior of such structures and its consequences on damage and design. This was achieved by utilizing single fiber tension and compression experimental data [10,11] implemented to extend a basal-plane-realignment based non-linear carbon fiber material model [8]. The applicability of the extended model to bending load cases was verified by implementing it into non-linear finite element (FE) simulations to predict the elastic response of the experiments and highlight its influence on strain distribution, neutral axis shift and stiffness. The technique was extended by an alternative, concise numerical algorithm, which allows to capture the elastic behavior without FE. The consequences of the novel elastic behavior on observed failure modes, especially on very thin shells that show remarkable flexibility, were revealed. Thus, an efficient design of highly deformable composite structures with failure prediction, becomes possible.

\* Corresponding author.

E-mail address: [arthursc@ethz.ch](mailto:arthursc@ethz.ch) (A. Schlothauer).

<sup>1</sup> A.S and G.P contributed equally.

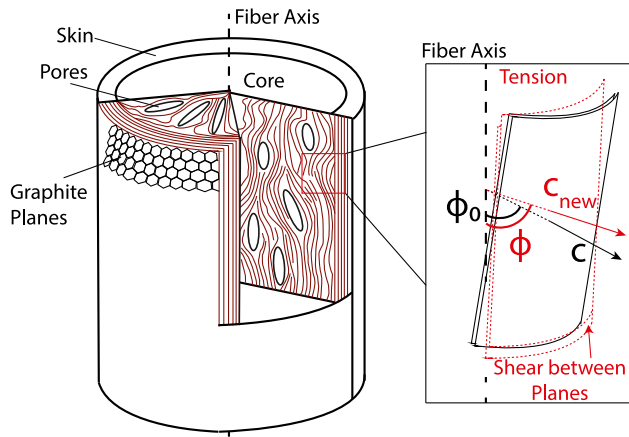


Fig. 1. Schematic (not to scale) of a PAN based CF, showing the nano-structure and pertinent features that affect the elastic response.

## 2. State-of-the-art in non-linear carbon fiber behavior

Some researchers in the past have approached non-linear CF behavior via polynomial stress–strain relations (strain energy density based) [7] while others utilized the reorientation of fibers' crystalline nano-structure [8] for constitutive modeling. Efforts were also applied in extending the latter work through mosaic models [12] or more recently with two-phase micro-mechanical modeling, considering amorphous and crystalline phases [9]. Although differing in grades of complexity, all modeling approaches pursue the same goal of matching the exact stress–strain relation of single-fiber tensile tests, which is showing an increasing fiber modulus with applied tensile strain, especially in Polyacrylonitrile (PAN)-based CFs.

The material model of Northolt et al. [8] bears physical meaning since it is based on the reorientation of graphitic basal planes that dominate the mechanical behavior. Fig. 1 illustrates the turbostratic structure of a PAN-based CF [13] consisting of a highly oriented skin with circumferentially aligned graphitic basal planes, and a less oriented crystalline fiber core. Upon tension, the initially misaligned graphitic layers with  $c$ -axis orientation,  $\phi_0$  (with respect to the fiber axis), reorient with increasing strain, causing an increase in the angle  $\phi$  and additionally shear between the graphitic basal planes. Hence, the CF constituent behavior is influenced by the angle  $\phi_0$ , the fiber's initial modulus,  $E_0$ , the in-plane modulus of a graphitic basal plane,  $e_1$ , as well as the shear modulus between the graphitic basal planes,  $g$ . According to [8], the aforementioned properties ( $E_0$ ,  $g$  and  $e_1$ ) can describe the strain–stress relation as in Eq. (1) (higher order terms are suppressed).

$$\epsilon = \frac{\sigma}{e_1} + \cos^2(\phi_0)[1 - \exp(-\frac{\sigma}{g})], \quad \cos^2(\phi_0) = g\left(\frac{1}{E_0} - \frac{1}{e_1}\right) \quad (1)$$

Although the tensile behavior was investigated and well matched by multiple studies over the last three decades, the compressive behavior of CF remains unclear. Yokozeki and Ishikawa observed increasing non-linearity in compression [14] at strains up to 1.5% that contributed to the reduction of the compressive strength of composite structures [15]. There, the compressive behavior was fitted using the polynomial strain energy density model [7], which was originally intended for single fiber tensile tests. Only recent findings by Ueda et al. [10,16] revealed the full extent of the compressive non-linearity. Single fiber compression tests show significantly higher non-linearity compared to tensile behavior, which, to date, has not been captured with existing models. Moreover, the impressive elasticity of the fiber in compression was observed with recoverable strains of up to ~5% and a total strain to failure of roughly 10%, making compressive fiber failure an unlikely event.

Formation of fiber micro-buckling, due to matrix shear yielding at low compressive strains, prevents the observation of these non-linearities in conventional thick composite structures [17]. However, pioneering work on ultra-thin composites by Murphey and collaborators [1,6,18] shows that these structures do not fail by said instabilities allowing the observation of non-linearity over a wider strain range. In that work, non-linear elastic response was approached by a semi-empirical model with different formulations for tensile and compressive response [5,19].

## 3. Materials and methods

To date, no analytical model was found to simultaneously represent tensile and compressive behavior of CF specimens subjected to high strains that matched experimental results. Therefore, a comprehensive approach for the efficient structural representation under large bending deformation was adopted. The initial hypothesis was that Northolt's material model (Eq. (1)) can, not only cover tension, but also compression, since it is based on the realignment of graphitic basal planes, regardless of loading direction. To prove this hypothesis, single CF constituent experimental data were initially used to derive its nano-structural parameters ( $E_0$ ,  $g$  and  $e_1$ ). This was followed by homogenization to composite level and implementation into numerical models. These were compared to shell-buckling tests, which, for the first time, allowed for the direct quantification of elastic non-linearities affecting strain distribution in tension and compression until failure. The applicability of the proposed concept was verified by the successful prediction of global response, local stress and strain distributions and its implications on failure.

### 3.1. Non-linear material modeling

The process of establishing the non-linear longitudinal UD lamina material behavior is described as follows: Firstly, existing representative single fiber experimental data [11] (tensile T700) and [16] (compressive T300) were fitted using Eq. (1) in the non-linear least squares Trust-Region minimization scheme of Matlab® 2019a, to obtain  $E_0$ ,  $e_1$ ,  $g$  for this CF family. Both fiber types are PAN based, of standard modulus and show similar nano-structure and stiffness. They mainly deviate in nitrogen content, surface characteristics and porosity [20] resulting in large difference of achievable strain, which is assumed not to influence the elastic response. Inversion of Eq. (1), to represent the stress response within the elastic domain for a given strain,  $\epsilon_i \in [-5\%, 2.1\%]$ , yields a non-analytical solution, approximated by the Lambert function  $W(x)$  as in Eq. (2).

$$\sigma_i(\epsilon_i) = \frac{E_0 \cdot g \cdot W\left(\frac{(e_1 - E_0) \cdot e^{-(-E_0 \cdot \epsilon_i + E_0 \cdot g - e_1 \cdot \epsilon_i) / (E_0 \cdot g)}}{E_0}\right) + E_0 \cdot e_1 \cdot \epsilon_i + E_0 \cdot g - e_1 \cdot g}{E_0} \quad (2)$$

Note that the numerical nature of this process requires tabulated values at different strains denoted by the index  $i$ . Next, an 'instant' fiber modulus, on the longitudinal direction can be calculated as  $E_{11,f,i}(\epsilon_{11,i}) = \sigma_{11,f,i} / \epsilon_{11,i}$  (indexes  $f$  and 11 are suppressed in Eq. (2)). Then, the rule of mixture was applied to evaluate the 'instant' modulus of the composite:

$$E_{11,i} = E_{11,f,i}(\epsilon_{11,i}) \cdot V_f + E_m \cdot (1 - V_f) \quad (3)$$

The matrix is considered linear isotropic with  $E_m = 3.4$  GPa based on [21] and a  $\nu_m = 0.35$ . Plastic yielding or viscoelastic effects are masked after homogenization in 1-direction, since fiber's stiffness dominates. For example, perfect elastoplastic response of the matrix in this direction has an impact of less than 0.5%.

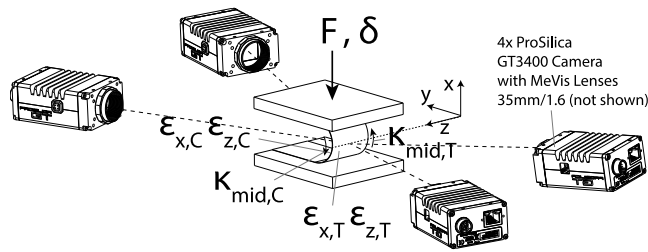


Fig. 2. Schematic of the setup for the large deformation shell buckling test (not to scale).

### 3.2. Testing procedure

To verify the modeling scheme within a highly non-linear regime, large deformation bending tests were conducted using a shell buckling test [1]. Two aluminum plates were traveling towards each other (plate displacement,  $\delta$ ) with 10 mm/min speed in a Zwick Roell universal testing machine. A specimen mounted in between the plates, gets buckled and forms an elliptical deformation curve (Figs. 2 & 3a). The desired buckling direction is enforced by an initial gentle manual push. During buckling, a barrier (step) in the plate (Fig. 3a) prevents the specimen from sliding out of the set-up. Folding forces ( $F$ ) were measured by a 5 kN load cell. The underlying strain and curvature distributions until failure were recorded with a two-sided 3D Digital Image Correlation (DIC) technique, which can cope with the occurring large displacements and capture the strains on highly curved surfaces. Strain gauges were not considered to avoid interaction with the very thin specimens. The dual DIC system (Fig. 2) was synchronized and jointly calibrated. DIC calibration parameters and the strain convergence analysis can be found in the Supplementary Material (SM), Section 1. Acquired data include tensile and compressive longitudinal ( $\epsilon_x$ , fiber orientation following the bending curvature) and transverse strains ( $\epsilon_z$ ) as well as curvatures ( $\kappa_{mid,C}$  &  $\kappa_{mid,T}$ ) on both sides of the specimen. The sampling rate of the DIC systems was 500 ms. Following noise and sensitivity analysis, this setup is able to capture strains with the precision of 0.02%. For more details the reader is referred to the SM - Section 1.

### 3.3. Specimen preparation

Thin-shell foldable composites are very prone to thickness variations [22]. Therefore, highest accuracy in specimen thickness, surface quality and fiber volume content was ensured by laminating  $30 \text{ g m}^{-2}$  Toray T700S CF and epoxy resin TP402 (NTPT Switzerland) in between two polished stainless steel plates following the manufacturers' autoclave cycle [21]. Four different specimen families were produced from four different plates of 4-, 5-, 10- and 13-ply UD-layups. A  $50 \mu\text{m}$  thick Polyimide release film (Airtech Thermalimide RCBS) provided a smooth surface finish while hardened stainless steel precision gauge strips prevented over-compaction and controlled thickness. Breather and peel-ply were absent in this process as they would introduce considerable surface imperfections resulting in non-negligible thickness variations in the thin shell composites. The composite plates were cut into  $L \times B = 100 \text{ mm} \times 40 \text{ mm}$  specimens. The width,  $B$ , was chosen to ensure uniform strain along the  $z$ -direction and length,  $L$ , to respect the depth of field of the lenses during buckling while allowing to achieve plate tangency during the main portion of the test. Fig. 3b shows the micrographs (using Keyence VHX6000 microscope) of specimens' sections obtained using standard metallographic techniques. The resulting thickness,  $t$ , was  $130 \pm 4 \mu\text{m}$ ,  $164 \pm 3 \mu\text{m}$ ,  $335 \pm 8 \mu\text{m}$  and  $403 \pm 7 \mu\text{m}$  with a fiber volume contents of 58%, 58%, 59% and 61% for the 4, 5, 10 and 13 ply samples, respectively. Thicknesses were measured using optical microscopy. Volume fractions were calculated with the

initial mass contents and verified using optical analysis (Matlab<sup>®</sup>) and thermogravimetric analysis (Pyris TGA<sup>®</sup>).

The specimens were airbrushed with a fine layer of acrylic paint of thickness  $t_p = 6.2 \pm 2 \mu\text{m}$  (measured with microscopy) to reduce reflections as well as to enable the creation of a fine and high-contrast speckle pattern used for the DIC analysis. A special stamp was utilized to introduce black  $170 \mu\text{m}^2$  speckles onto the specimen. Subset and step size ensuring strain convergence of the DIC analysis were found to be at  $11 \text{ px}^2$  and  $4 \text{ px}^2$ , respectively, with a virtual strain gauge area of  $2 \text{ mm}^2$  (in Vic3D v7, see SM - Section 1). All data points along the line of highest curvature were averaged to reduce measurement noise. For a given curvature and strain on both sides of the specimens, one can directly calculate the neutral axis position ( $\hat{y}_{na}$ ) and hence the relative neutral axis shift ( $S_{rel}$ ) compared to a linear material behavior ( $\hat{y}_{na,lin} = \frac{t}{2}$ , see Figure in Section 3.5), according to Eq. (4). Linear strain distribution over the specimen thickness (Euler-Bernoulli) is expected to be valid, as the relation  $\frac{1}{\kappa_{mid,T}} = \frac{1}{\kappa_{mid,C}} + t$  was confirmed in all experiments. Consequently, hereafter the shell curvature will be referred to as  $\kappa_{mid} = \frac{\kappa_{mid,T} + \kappa_{mid,C}}{2}$ .

$$S_{rel} = 1 - \frac{\hat{y}_{na}}{\hat{y}_{na,lin}} = \frac{(\epsilon_{x,C} + \epsilon_{x,T})}{(\epsilon_{x,C} - \epsilon_{x,T})} \quad (4)$$

The influence of non-bending related compressive strains due to the load introduction is negligible (up to 0.023%, as stated in the SM - Section 2). The strain on the (tensile or compressive) composite surface,  $\epsilon_x$ , was obtained by correcting the measured longitudinal strain data from the DIC system,  $\epsilon_{x,DIC}$ , considering that this is practically the strain measured on the additional thickness of acrylic paint, as:

$$|\epsilon_x| = |\epsilon_{x,DIC}| - \kappa_{mid} \cdot t_p \quad (5)$$

The obtained strain field also allows for the evaluation of Poisson's effect during testing. At every curvature, the corresponding effective Poisson's ratio on both sides of the specimen was calculated with Eq. (6).

$$v_{eff} = -\frac{d\epsilon_x}{d\epsilon_z} \quad (6)$$

The derivatives were obtained using a finite difference scheme. Due to the low transverse strain values compared with the measuring noise (values below 0.02% were not evaluated, see Section 3.2),  $v_{eff}$  and  $\epsilon_z$  had to be smoothed using a moving average filter. Elastic response was studied up to initial damage events. These events were recognized by kinks in the  $F - \delta$  behavior. To exclude parasitic effects (e.g. slipping), damage events were verified by visual inspection of the DIC images. For the failure analysis, the failure point was defined as the peak point of the  $F - \delta$  behavior.

### 3.4. Finite element analysis

The estimated material non-linear response derived from the aforementioned procedure was implemented in FE modeling using Abaqus Standard v6.12 to predict the experimental response. In these models the geometry of the loading plates was approximated by two, 2 mm thick aluminum solid sections discretized using linear brick, reduced integration elements (C3D8R) with the boundary conditions indicated in Fig. 4. Thus, no bending was allowed. The plates could deform on the free surface enabling the development of contact stresses. The specimens were modeled as thin shells using 3D reduced integration, shell elements (S4R), assuming plane stress approximation. To model the non-linear elastic material response in the longitudinal direction, orthotropic lamina engineering constants where implemented in a tabular form ( $\sim 220$  entries), allowing only  $E_{11,i}$  to vary with a dependency in  $\epsilon_x$ , employing the user defined field option (-USDFLD-) and a Fortran based subroutine. Thus, the longitudinal stresses are evaluated as  $\sigma_x = E_{11,i}(\epsilon_{x,i}) \cdot \epsilon_x$  for every increment. The remaining engineering constants of the composite lamina were approximated with the Halpin-Tsai

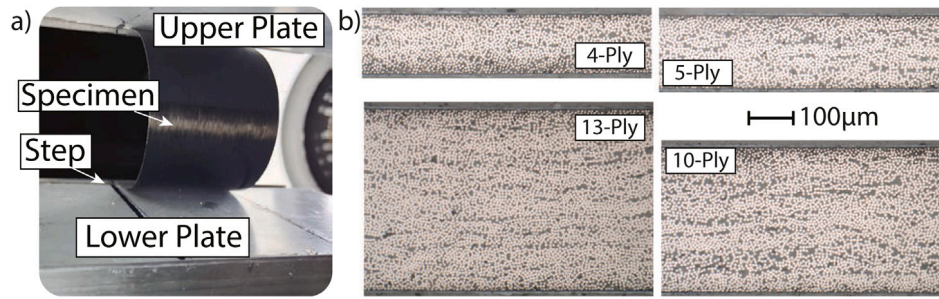


Fig. 3. (a) Image of a 164  $\mu\text{m}$  specimen undergoing flexural testing. (b) Representative micrographs of the specimens. A fine layer of acrylic paint used for DIC analysis can be seen on the micrographs.

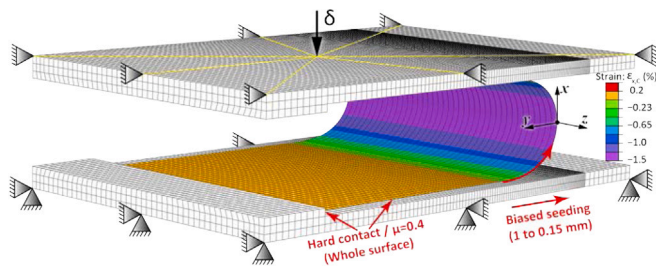


Fig. 4. FE of the conducted shell buckling experiments illustrating boundary conditions and mesh size. Displayed are the maximum compressive strains of a 5-Ply specimen (Comparable with Fig. 7) for equivalent  $\delta$ . Note that  $x$ ,  $y$  and  $z$  are local coordinates here.

micromechanical semi-empirical corrections [23] ( $\xi_1 = 2$  for  $E_{22}$ ,  $\xi_2 = 1$  for  $G_{12}$ ), for fiber properties obtained from [24]. The corresponding calculated constants for  $V_f = 58\%$  are:  $E_{22} = 8$  GPa,  $G_{12} = 4.05$  GPa,  $G_{13} = 2.6$  GPa,  $\nu_{12} = 0.31$  and  $\nu_{23} = 0.43$ . For simplicity, these properties were considered independent of the applied strain given that the load is predominantly longitudinal. In order to allow the non-linear through-thickness stress profile, the shell section was discretized in 20 layers with 3 integration points each (Simpson rule), using the composite layup option of Abaqus with the aforementioned material constants dependency. For every tested thickness, layer thickness was adapted accordingly. This approach allowed the variation of  $E_{11,i}$  within shell's thickness depending on the imposed strain, and moreover allowed the neutral axis to be defined based on laminate theory framework. A hard contact (no penetration) algorithm with a tangential friction coefficient  $\mu = 0.4$  was implemented between the plate surface and the outer surface of the shell-specimen, in order to mimic the actual testing conditions as close as possible (also allowing separation). The barrier (step) in the aluminum plates is also adopted in the model, preventing slipping. The included tangential friction promotes convergence and is expected to have no influence on the response as the barrier constrains the maximum slip (less than 2.5  $\mu\text{m}$  according to the simulation). A bias seeding of the mesh was employed to ensure that even at the minimum flexural radius ( $\sim 2$  mm) at least 13 elements existed. This value was derived after convergence analysis. The surface of the solid plates followed the same mesh pattern to facilitate the contact algorithm (see Fig. 4). An initial step that causes buckling initiation was implemented in the simulation with the shell forced to follow Euler's first buckling mode:  $C \cdot \sin\left[\frac{\pi \cdot \frac{L}{2} + |x|}{L}\right]$  with  $C = 2$  mm. The choice of initial buckling amplitude is not expected to affect the FE model.  $C$  was chosen after parameter variations within 1–5 mm to achieve the desired buckling direction and contact initialization.

### 3.5. Concise numerical algorithm

A computationally efficient approach for determining neutral axis and stress distribution, not requiring FE modeling, can be utilized assuming pure moment conditions during the shell buckling experiment. For an Euler–Bernoulli beam, i.e.  $\epsilon = -\kappa y$  (see Fig. 5a),  $\sigma(y)$  and  $y_{na}$  for a given  $\kappa$  were calculated using the process illustrated in Fig. 5b and described as follows: For a given  $\kappa$  and  $t$  the linear through-thickness strain profile designates a stress profile that follows Eq. (2). The actual stress distribution and neutral axis position is found by minimizing  $\int_0^t \sigma(\hat{y}) d\hat{y} \rightarrow 0$ , to fulfill the equilibrium condition on the  $x$ -axis, i.e.  $\sum F_x = 0$ . The script for the calculation is written in Matlab<sup>®</sup> 2019a, employing the 'fzero' function. The thickness is discretized in 100 increments while the integral is calculated by the trapezoidal rule.

## 4. Results and discussion

### 4.1. Material model

The stress–strain behavior of a CF as well as the respective fits with Eq. (1) can be seen in Fig. 6. The corresponding fitting parameters with the 95% confidence bounds can be found in Table 1. The resulting initial crystallite orientation parameter  $\cos^2\phi_0$  was calculated accordingly. For comparison, the fit of solely the tensile regime [11] is also included.

The fit of the full range (tension/compression) predicts a softer  $e_1$  as well as a drastically lower shear modulus between the graphitic basal planes ( $g$ ) compared with values for PAN based CFs reported in the literature [8,25]. Note that literature values for  $g$  were previously determined on tensile testing data of fibers by fitting  $\cos(\phi_0)$  in Eq. (1), based on highly scattered data. Given the marginal stiffening of the fibers in tension (from 216 to 230 GPa, see Fig. 6b), the quality of this fit is doubtful as also demonstrated by the very wide 95% confidence bounds of  $e_1$  and  $g$  in Table 1. In fact, the values listed in the corresponding row resemble the initial guess, which was based on [8].

Considering the full range fit, the compressive softening has the highest impact on the identification of  $e_1$  and  $g$ . The higher the  $g$ , the larger the shear stiffness in-between the basal planes and hence the more linear the response, as can be seen in Eq. (1) (for  $g \rightarrow \infty$  the non-linear part of the equation vanishes). Thus, the high non-linearity in compression can only be captured with the relatively low value identified herein. This value compares well to values determined by static and ultrasonic experimental techniques [26] on pyrolytic single crystal graphite. Notably, the full range fit is still able to depict the tensile response with minimal deviation, while the compressive softening, clearly dominant over the tensile stiffening, is well captured. It is striking, that the maximum fiber modulus,  $E_{11,f,max}$ , tends to the identified  $e_1$ . This relates to the fact that tension leads to alignment of the graphitic basal planes with the loading direction. Thus, after a certain point and on, the realignment saturates. The in-plane modulus of perfect, single crystal graphite is about four times higher than the

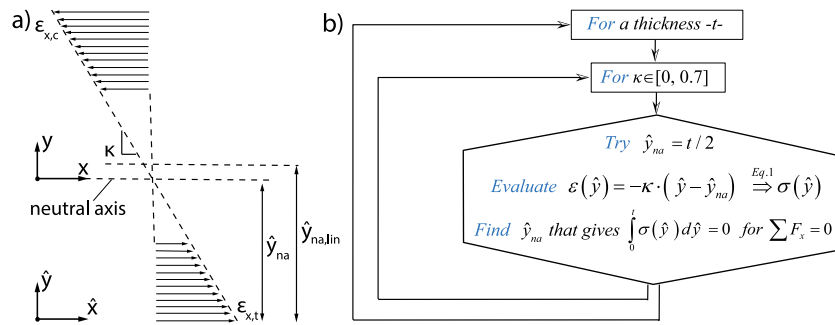


Fig. 5. (a) Strain distribution within the specimen assuming Euler-Bernoulli beam theory. (b) Numerical process of calculating the strain and corresponding stress distribution in the specimen.

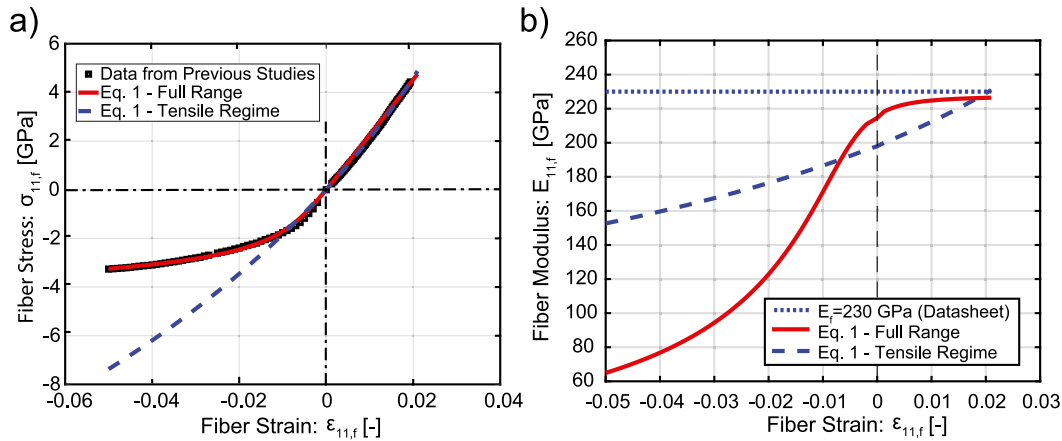


Fig. 6. Tensile and compressive test data from [11,16] fitted with Eq. (1). One fit only respects the tensile behavior while the other fits the full range.

Table 1

Fitting parameters of the constants in Eq. (1) with 95% confidence bounds. Subscripted values indicate the lower confidence bound, while superscripted values indicate the upper bound.  $E_0$  denotes the fiber initial modulus,  $e_1$  the effective in-plane modulus of the graphitic basal planes,  $g$  the shear modulus in between the graphitic basal planes and  $\cos^2(\phi_0)$  the resulting orientation parameter. The linear elastic value results from a linear fit according to ASTM D 3379-75, i.e. chord modulus, in [11] matched datasheet value of 230 GPa.

Type of fit	$E_0$ [GPa]	$e_1$ [GPa]	$g$ [GPa]	$\cos^2(\phi_0)$ [-]	$\phi_0$ [deg]
Eq. (1) Full range fit	216 <sup>3</sup> <sub>-3</sub>	228 <sup>4</sup> <sub>-4</sub>	0.588 <sup>0.02</sup> <sub>-0.02</sub>	0.00014	89.3
Eq. (1) Tensile regime fit	196.5 <sup>5.2</sup> <sub>-5.3</sub>	1182 <sup>1.94e+04</sup> <sub>-1.48e+04</sub>	11.55 <sup>62.41</sup> <sub>-16.2</sub>	0.049	77.2
Linear elastic (fit from [11])	230.5	-	-	-	-

value in the first row of Table 1 [8]. Consequently,  $e_1$  represents an effective in-plane modulus of a graphitic layer with imperfect microcrystalline structure [13]. Hence, an initial guess for this parameter shall be the highest recorded modulus of the fiber.

Overall, the model captures the tensile [11] and compressive behavior [16] with a maximum deviation of  $\approx 3\%$ . The confidence bounds of the full range fit are narrow, indicating high sensitivity with the parameters of Eq. (1). The values in Table 1 were implemented in Eqs. (2) & (3) and utilized in the FE and the concise numerical scheme. The results were compared with the experimental elastic response.

#### 4.2. Elastic response

To evaluate the behavior of a thin CF-reinforced specimen in bending, the force-curvature as well as the strain data from the DIC were considered. The DIC results from both camera systems can be seen in Fig. 7a, in increments from the moment the specimen reaches tangency with the plate, until shortly before failure. The DIC results reveal a uniform strain distribution over the width, confirming the choice of  $B$ . Moreover, a clearly discernible strain peak can be captured with the DIC in the middle of the flexure. Following the DIC strain convergence analysis (SM — Section 1), the highly strained area is sufficiently large

to capture the highest strain peak. Furthermore, the material non-linearity becomes evident by the neutral axis shift towards the tensile side as seen in the increasing compressive strain as the experiment advances. The evolution of nominal through-thickness strain distribution at the line of highest curvature on both specimen sides, can be found in Fig. 7b. No significant dependency on thickness with respect to non-linear behavior is observed. As a consequence of the compressive softening and the corresponding neutral axis shift, compressive strains in thin specimens reach up to 3%. This is significantly higher than the finding of other studies with thicker unidirectional specimen [18,27], where measured compressive strains were limited to lower values (around 2.2%), due to fiber micro-buckling.

The required forces normalized with the second moment of inertia ( $F/I$ ) versus specimen's curvature are shown in Fig. 8, and are compared with the FE models using the different parameter sets in Table 1. Note that the complex buckling shape in this test does not allow for the direct measurement or analytical estimation of folding moments without assuming a governing material law. Fig. 8 clearly indicates that a linear material model drastically overestimates specimen's stiffness and hence folding forces. The reported values that solely match fiber tensile test data are also clearly overestimating the stiffness. Only the full range fit, that assembles compressive and tensile behavior of a

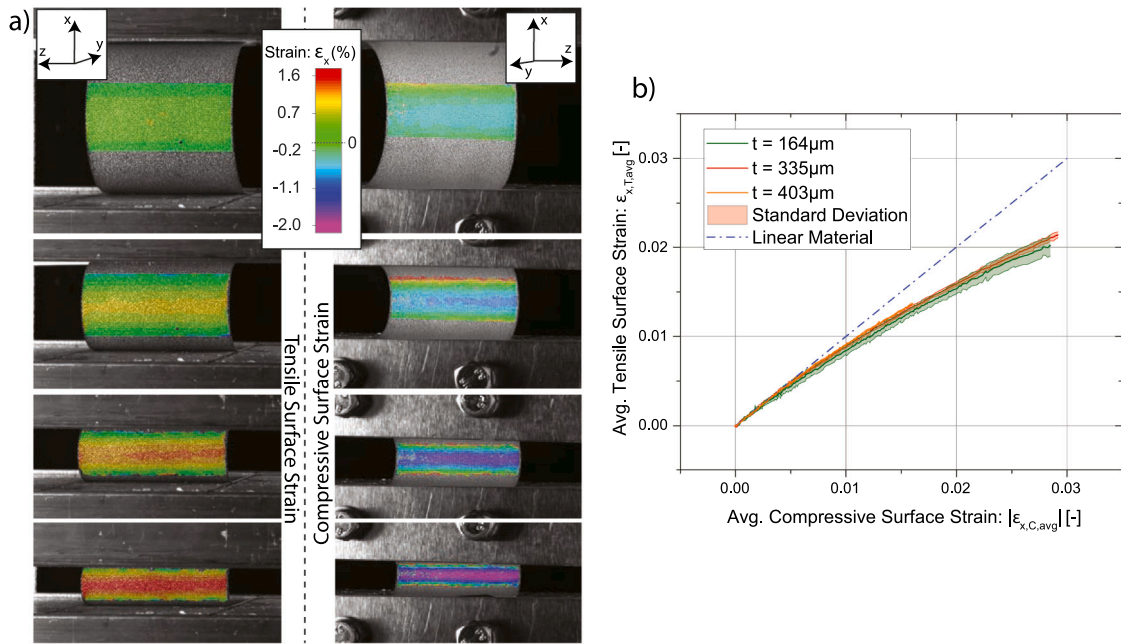


Fig. 7. (a) Strain distribution over a 5-ply specimen at different stages of the shell buckling test on the tensile (left) and compressive side (right). (b) Strain measurements of the tensile surface plotted against the strain on the compressive surface. The plot shows the behavior for 3 different thicknesses, averaged over 5 specimen per thickness. The shaded region indicates the standard deviation of 5 specimens.

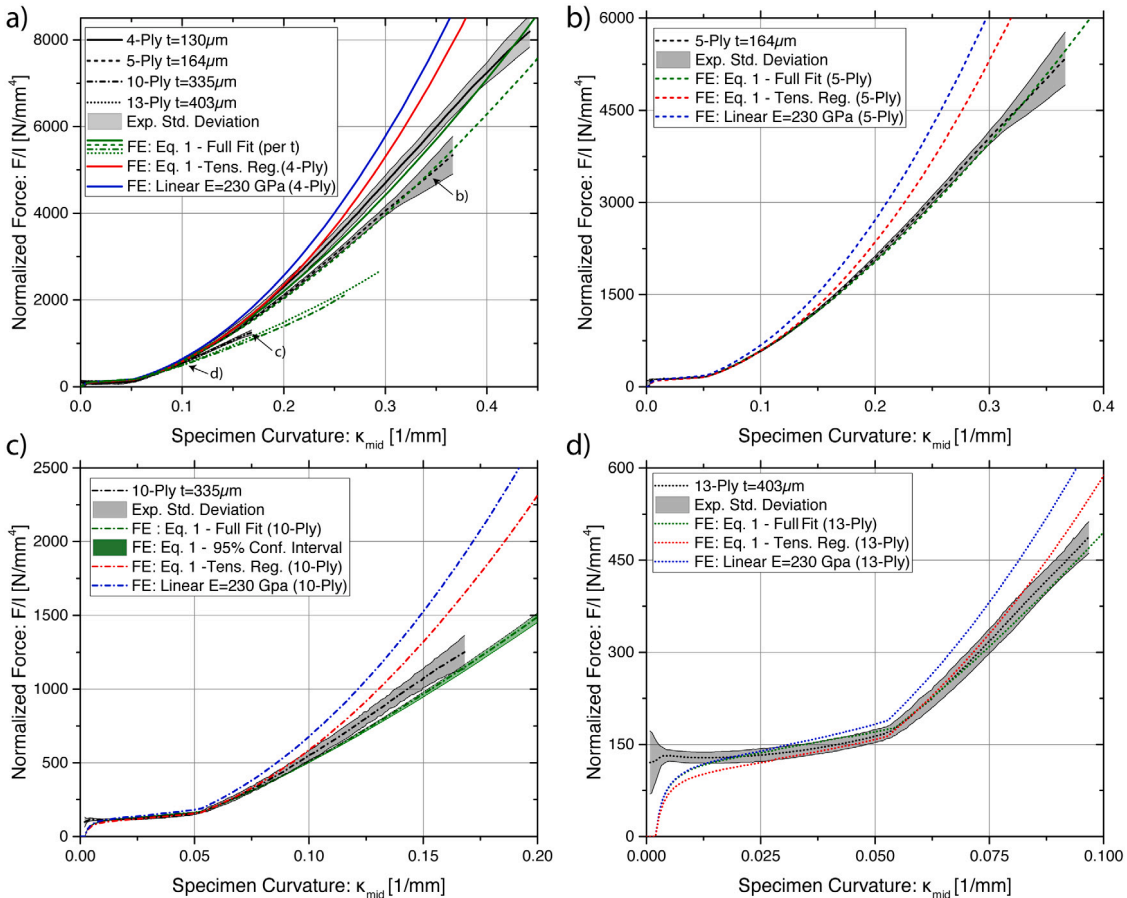


Fig. 8. Normalized Force–Curvature relations during shell buckling test averaged over five specimen per thickness. The results are compared with FE for different fitting parameters of Eq. (1) (see Table 1). (b)–(d) show a detailed view of the different thicknesses and their comparison with the respective simulations.

single fiber [11,16] matches the  $F/I - \kappa$  behavior. The agreement is better for very thin specimens (4- and 5-ply) where resin bleed and

fiber volume content were well controlled, while for thicker specimen a slightly higher standard deviation can be observed. Overall, the highly

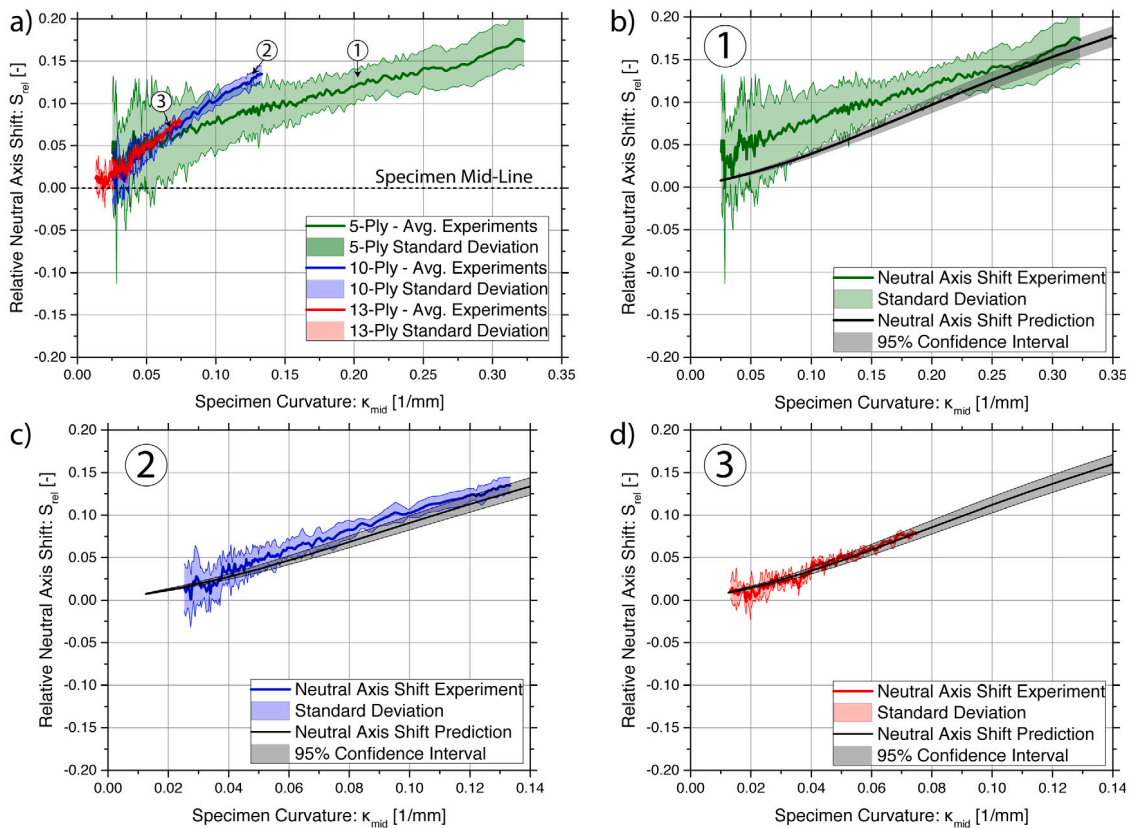


Fig. 9. (a) Measured neutral axis shift for different specimen thicknesses averaged over all specimens per family. (b–d) Detailed view on the respective thicknesses from (a) compared to the numerical algorithm (Fig. 5). Gray regions indicate the 95% confidence region of the fit (Table 1). (For interpretation of the references to color in this figure legend, the reader is referred to the web version of this article.)

non-linear nature of this CF family in compression was confirmed, which results in a drastic reduction of stiffness at very high curvatures. Note that the overall stiffness behavior remains practically unaffected within the 95% confidence bounds (see Fig. 8c).

The measurements of the non-linearity-induced neutral axis shift in specimens of different thickness can be found in Fig. 9(a). These are compared with the prediction of the neutral axis shift using the concise numerical algorithm in Fig. 9(b) to (d). At high curvatures, the neutral axis shifts up to ~17% towards the tensile side of the specimen, due to CF non-linearity. The very small bending radii of 5-ply specimen result in a higher standard deviation due to larger measurement difficulties related to the limited field of view, an effect that is reduced in 10- and 13-ply specimens. The neutral axis shift prediction based on the numerical algorithm agrees well with the measurements of the DIC, validating the material modeling approach.

As shown in Fig. 10, the numerical algorithm (Fig. 5) as well as the FE agree well in predicting the through-thickness stress distribution. The fiber softening effectively decreases stress gradients on the compressive side leaving more fibers exposed to high strains. Slight deviations can be explained due to the pure moment assumption on the numerical algorithm, which is not completely met by the experiment or the FE, as compressive loads induce buckling (see SM — Section 2).

### 4.3. Failure response

The force–displacement curves of 3 exemplary specimens per thickness and the corresponding DIC pictures for selected points can be found in Fig. 11a & b. The initial failure in all specimens except the 13-ply, coincides with the maximum force, i.e. initial ≡ ultimate failure. The 13-ply specimens shows subsequent damage events, identifiable by localized blister formation on the compressive surface, seen as

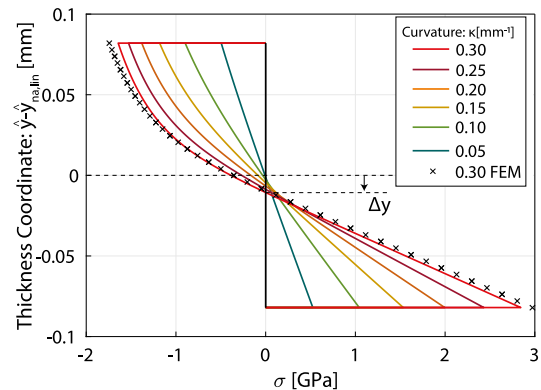
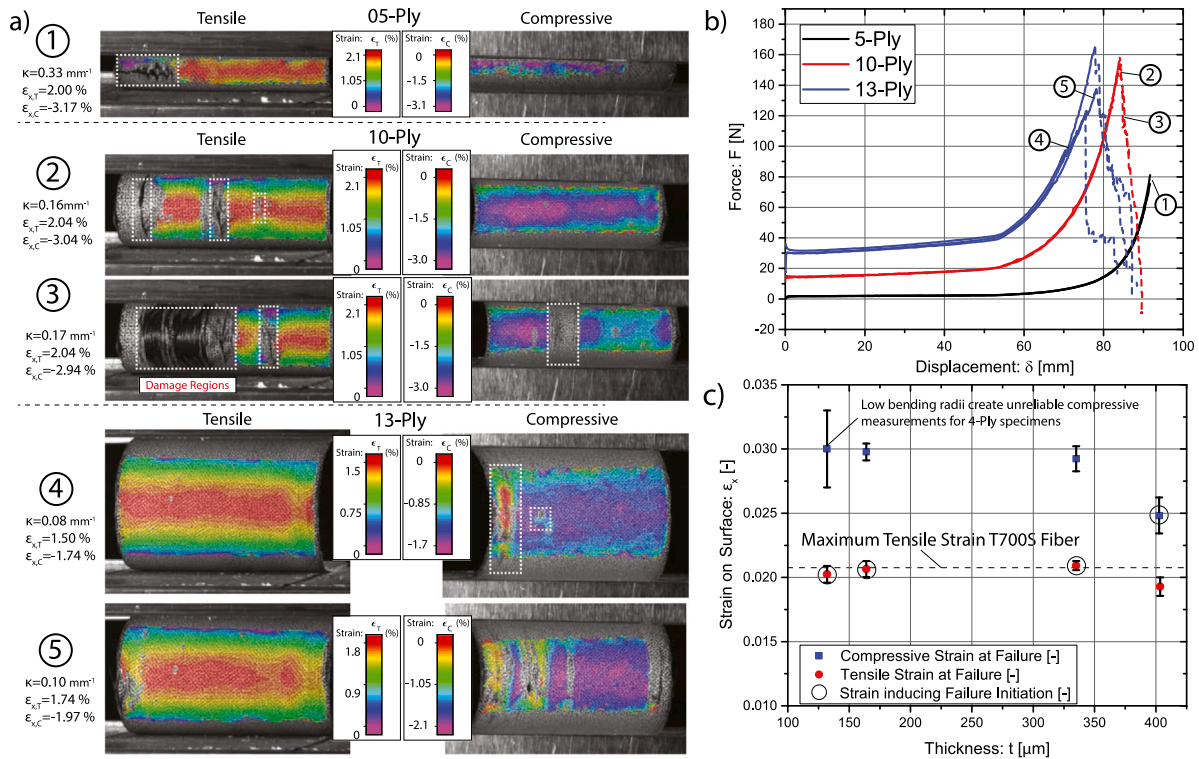


Fig. 10. Estimated through-thickness stress distribution exemplary for 5-Ply specimens at different curvatures computed with the concise numerical algorithm compared to the corresponding result from the FE at  $\kappa = 0.30 \text{ mm}^{-1}$ .

load-drops in the  $F - \delta$  graph. Substantial blistering leads to ultimate failure.

Fig. 11a illustrates discernible initiation of failure events and their progression. 10-ply specimens initiate failure from the tensile side noticeable through a sharp drop in the  $F - \delta$  graph and clearly visible fiber breakage at  $\kappa = 0.16 \text{ mm}^{-1}$  (Point ②). The compression side stayed intact at roughly 3% compressive strain. At  $\kappa = 0.17 \text{ mm}^{-1}$  (Point ③) the damage reached the compressive side by means of first cracks (fiber splitting) attributed to the large release of elastic energy from the tensile fiber rupture. At this point, already more than 30% of the visible area of the tensile side had failed completely. A stagnation of





**Fig. 11.** (a) DIC pictures showing visible failure of the specimens with given strain and curvature values at the specific moment the pictures were taken. (b)  $F - \delta$  curves of 3 specimen per thickness. Initial loads correspond to the load needed to induce buckling of the respective thickness. Points indicated correspond to the pictures in (a). Dashed lines indicate values after failure. (c) Average strain at catastrophic failure of all specimens measured at both sides of the bent specimen as a function of thickness.

the measured compressive strains on the intact domains was observed due to the failure-induced shift of the neutral axis (back) towards the symmetry plane. The  $\sim 70 \mu\text{m}$  thicker 13-ply specimens show a bifurcation in failure behavior. At  $\kappa = 0.08 \text{ mm}^{-1}$  (Point ④), blisters formed on the compression side, highlighted by white rectangles in Fig. 11a. The tensile side, being below tensile failure strain, stayed intact during substantial blistering and cracking (a slight change in the tensile strain distribution behind the blister can be seen). Hence, the compressive strain at catastrophic failure does not reach the values of the thinner specimen.

Fig. 11c summarizes the strains at catastrophic failure as a function of thickness. Fiber tensile strain to failure (2.1% according to manufacturer) defined the failure for specimen with thickness up to  $335 \mu\text{m}$ . Hence, for very thin, highly deformable structures, a maximum fiber-tensile-strain criterion is suitable for estimating the achievable curvature, after having accounted for non-linear constitutive behavior. Neutral axis shift further delays the formation of high strains on the tensile side leading to higher achievable curvatures. This effect is even more pronounced for fiber types with high maximum tensile strain like T700S. The trend changes for thicker specimens, which are not able to achieve the maximum tensile fiber strain before compressive failure (micro-buckling formation) is initiated, indicated by the overall lower tensile and compressive strains at failure. Consequently, bending stress gradients, which have been shown to affect the formation of micro-buckling [27], can ultimately prevent compressive failure initiation. Note that non-linear constitutive behavior reduces the compressive stress gradients close to the surface at high strains (Fig. 10). The failure mechanism bifurcation point was identified for thicknesses between  $335 \mu\text{m}$ – $410 \mu\text{m}$  for the given material combination. Further thickness increase is expected to lead to further reduction in critical failure strain, converging to data reported for typical thicknesses in standardized composite testing. For an accurate prediction of the bifurcation point, further investigations are required.

Given the large compressive strains in all specimens, one cannot neglect transverse failure modes from Poisson's effects, as the transverse tensile strength of composites is known to be low, leading to potential transverse cracking or splitting [28]. Note that the term transverse cracking refers to damage caused by transverse loading, usually related to fiber-matrix-interface failure or brittle matrix failure. Fig. 12 illustrates the relation between longitudinal and transverse strains and the associated Poisson's effect (Eq. (6)) during the shell buckling tests, in exemplary 5-ply (Fig. 12a) and 10-ply specimens (Fig. 12b). Once tangency is established, none of these specimens reaches the expected  $\nu_{12} = 0.31$  (Section 3.4), which is attributed to boundary effects. The higher the curvature, the shorter the arc length in between load application points. The shorter the arc length in between load application, the larger the influence of boundary effects such as friction locking. Thicker specimens such as 10-ply in Fig. 12b, which intuitively achieve higher longitudinal strains at lower curvatures, also exhibit higher transverse strains as the influence of boundary effects decreases with increasing free arc length. However, with increasing curvature (around 1.3% longitudinal strain) the influence of boundary effects increases indicated by a stagnating  $\nu_{eff}$ . The 5-ply specimen in Fig. 12a does not show such behavior, as the significantly lower curvatures constantly cause friction locking effects and constrain transverse strains. Consequently, boundary effects suppress transverse failure mechanisms in highly deformable composites. Note that the effect of fibers nano-structure rearrangement on the Poisson's ratio cannot be resolved by such measurements and further investigations are required.

#### 4.4. Non linear effects and elastic recovery

Many highly deformable composite structures necessitate full elastic recovery as in stowage and deployment of foldable structures. To verify the extend of elastic response and discern non-recoverable non-linear effects, some specimens were loaded to tensile strain levels up to 85% of their maximum sustained curvature, and then unloaded before

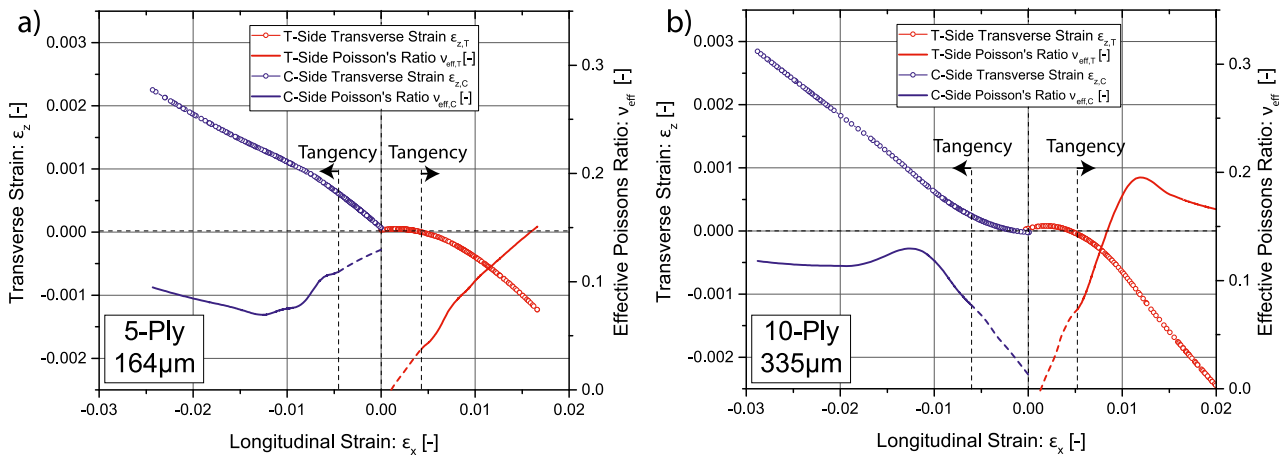


Fig. 12. Comparison between transverse-, longitudinal strain and effective Poisson's ratio of a 5-ply specimen (a) and a 10-ply specimen (b). Red lines and markers indicate the tensile side, whereas blue indicate the compression side. Dashed domains represent measurements before tangency. (For interpretation of the references to color in this figure legend, the reader is referred to the web version of this article.)

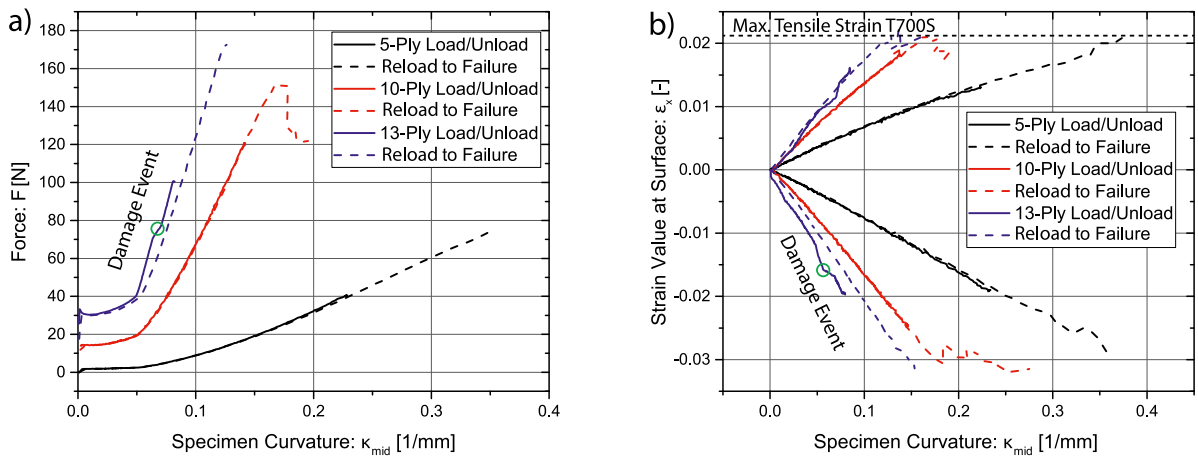


Fig. 13. Force–Curvature (a) and Strain–Curvature plots (b) of 3 specimens of different thickness. The solid lines indicate a first loading step to induce tensile strain levels of approximately 1.3–1.8%. Reloading till failure is indicated by the dashed line.

being reloaded until failure. The value of 85% is marginally out of the standard deviation of the ultimate failure values. Reloading was performed right after unloading, as this study serves to reveal the extend of elastic non-linearity. Long-term creeping or cyclic effects, even though important, were not within the scope of this study. The force–curvature as well as the strain–curvature plots of these experiments can be seen in Fig. 13. The thinner specimens were able to follow the initial strain and force paths indicating a fully elastic recovery. Only the 13-ply specimens showed a damage event resulting in a discontinuity of the respective curves. After reloading, a decrease in stiffness could be observed in Fig. 13a. The damage event, in the form of micro-buckling/fiber blister formation, was identified on the compressive side, also showing different strain–curvature behavior upon reloading Fig. 13b. The 13-ply thick specimen appears to be close to the bifurcation point between tensile and compressive failure for the given fiber matrix combination, as this specimen was able to reach the maximum tensile strain without any additional damage events upon reloading. The results show that the observed non-linearity is fully reversible for very thin structures, recovering the initial structural stiffness once deformation is removed.

### 5. Conclusions

Accurate measurements of strain distributions and elastic response of UD thin shell composites in bending until failure have shown that

elastic non-linearity, especially in the compressive regime, is of much higher extent than generally acknowledged. This is especially exposed in very thin composite shells where compressive strains of up to 3% without failure are observable. Linear material models or non-linear material models fitted solely on tensile testing, fail to match local strain distribution as well as global stiffness response. This leads to drastic over prediction of required folding forces and drastic under prediction of structure's achievable curvature until failure.

This work demonstrated that Northolt's CF material model, which accounts for the realignment of the graphitic basal planes in tension [8], can be successfully extended to describe highly non-linear compressive constituent behavior [10]. This makes it suitable for bending load cases. However, precise representation of the complete regime (tension/compression) lead to re-evaluation of the nano-structural properties of the model ( $E_0$ ,  $g$ ,  $e_1$ ). Consequently, homogenization to composite level and implementation into numerical models can accurately predict stress distribution, neutral axis shift and global stiffness response in highly deformable thin shell structures, as corroborated by the conducted experiments.

The identified elastic behavior has drastic implications on the failure of such structures. Fiber tensile failure was observed as damage driving mechanism for very thin shells and occurred at maximum fiber

tensile strain. This failure is significantly delayed by the compressive-softening-induced neutral axis shift, allowing for an remarkable flexibility in UD CF composite shells. Taking full advantage of fiber's tensile strength is only feasible due to the suppression of compressive failure. The latter may be influenced by the reduced stresses and stress-gradients at high curvatures caused by non-linearity. Notably transverse cracking is also hindered in structures subjected to high bending curvatures due to friction locking at the load application points. Nevertheless, establishment of predictive modeling of the transition of failure modes, respecting the thickness dependence, needs further investigation. The proposed material modeling approach is suitable for treating and designing highly deformable, fully elastically recoverable composite shells with compressive strains as high as 3%, covering the full structural response until failure, especially when thin enough to be dictated by tensile failure initiation. This approach can be efficiently utilized to design deployable structures, flexible meta-materials or novel applications, where high elastic flexibility at low extensibility is required.

### CRedit authorship contribution statement

**Arthur Schlothauer:** Data curation, Conceptualization, Writing, Experiments and modelling. **Georgios A. Pappas:** Data curation, Conceptualization, Writing, Experiments and modelling. **Paolo Ermanni:** Supervision, Conceptualization, Writing - review & editing.

### Declaration of competing interest

The authors declare that they have no known competing financial interests or personal relationships that could have appeared to influence the work reported in this paper.

### Acknowledgments

The research was supported by the ETH-board SFA-Grant "Advanced Manufacturing" as well as the SNF REquip program, SNF206021 150729, for the acquisition of the DIC.

### Appendix A. Supplementary data

Supplementary material related to this article can be found online at <https://doi.org/10.1016/j.compscitech.2020.108378>.

### References

- [1] G. Sanford, A. Biskner, T. Murphey, Large strain behavior of thin unidirectional composite flexures, in: Proceedings of the 51st AIAA/ASME/ASCE/AHS/ASC Structures, Structural Dynamics, and Materials Conference, (April) 2010, <http://dx.doi.org/10.2514/6.2010-2698>.
- [2] M.R.M. Hashemi, A.C. Fikes, M. Gal-katziri, B. Abiri, F. Bohn, A. Safaripour, M.D. Kelzenberg, E.L. Warmann, P. Espinet, N. Vaidya, E.E. Gdoutos, C. Leclerc, F. Royer, S. Pellegrino, H.A. Atwater, A. Hajimiri, A flexible phased array system with low areal mass density, *Nat. Electron.* 2 (May) (2019) 195–205, <http://dx.doi.org/10.1038/s41928-019-0247-9>.
- [3] A. Schlothauer, P. Ermanni, Stiff composite cylinders for extremely expandable structures, *Sci. Rep.* 9 (1) (2019) 1–8, <http://dx.doi.org/10.1038/s41598-019-51529-7>.
- [4] M. Sakovsky, P. Ermanni, A thin-shell shape adaptable composite metamaterial, *Compos. Struct.* 246 (February) (2020) 112390, <http://dx.doi.org/10.1016/j.comstruct.2020.112390>.
- [5] T.W. Murphey, M.E. Peterson, M.M. Grigoriev, Large strain four-point bending of thin unidirectional composites, *J. Spacecr. Rockets* 52 (3) (2015) 882–895, <http://dx.doi.org/10.2514/1.A32841>.
- [6] T.W. Murphey, W. Francis, B. Davis, J.M. Mejia-Ariza, High strain composites, in: 2nd AIAA Spacecraft Structures Conference, 2015, pp. 1–53, <http://dx.doi.org/10.2514/6.2015-0942>.
- [7] T. Ishikawa, M. Matsushima, Y. Hayashi, Hardening non-linear behaviour in longitudinal tension of unidirectional carbon composites, *J. Mater. Sci.* 20 (11) (1985) 4075–4083, <http://dx.doi.org/10.1007/BF00552401>.
- [8] M.G. Northolt, L.H. Veldhuizen, H. Jansen, Tensile deformation of carbon fibers and the relationship with the modulus for shear between the basal planes, *Carbon* 29 (8) (1991) 1267–1279, [http://dx.doi.org/10.1016/0008-6223\(91\)90046-L](http://dx.doi.org/10.1016/0008-6223(91)90046-L).
- [9] F. Tanaka, T. Okabe, H. Okuda, M. Ise, I.A. Kinloch, T. Mori, R.J. Young, The effect of nanostructure upon the deformation micromechanics of carbon fibres, *Carbon* 52 (2013) 372–378, <http://dx.doi.org/10.1016/j.carbon.2012.09.047>.
- [10] M. Ueda, W. Saito, R. Imahori, D. Kanazawa, T.K. Jeong, Longitudinal direct compression test of a single carbon fiber in a scanning electron microscope, *Composites A* 67 (2014) 96–101, <http://dx.doi.org/10.1016/j.compositesa.2014.08.021>.
- [11] T. Langston, The tensile behavior of high-strength carbon fibers, *Microsc. Microanal.* 22 (4) (2016) 841–844, <http://dx.doi.org/10.1017/S143192761601134X>.
- [12] M. Shioya, E. Hayakawa, A. Takaku, Non-hookean stress-strain response and changes in crystallite orientation of carbon fibres, *J. Mater. Sci.* 31 (17) (1996) 4521–4532, <http://dx.doi.org/10.1007/BF00366347>.
- [13] F. Barnet, M. Norr, A three-dimensional structural model for a high modulus pan-based carbon fibre, (April) 1976, pp. 93–99, [http://dx.doi.org/10.1016/0010-4361\(76\)90019-7](http://dx.doi.org/10.1016/0010-4361(76)90019-7).
- [14] T. Yokozeki, S. Ogihara, S. Yoshida, T. Ogasawara, Simple constitutive model for nonlinear response of fiber-reinforced composites with loading-directional dependence, *Compos. Sci. Technol.* 67 (1) (2007) 111–118, <http://dx.doi.org/10.1016/j.compscitech.2006.03.024>.
- [15] T. Yokozeki, T. Ogasawara, T. Ishikawa, Effects of fiber nonlinear properties on the compressive strength prediction of unidirectional carbon-fiber composites, *Compos. Sci. Technol.* 65 (14) (2005) 2140–2147, <http://dx.doi.org/10.1016/j.compscitech.2005.05.005>.
- [16] M. Ueda, M. Akiyama, Compression test of a single carbon fiber in a scanning electron microscope and its evaluation via finite element analysis, *Adv. Compos. Mater.* 28 (1) (2019) 57–71, <http://dx.doi.org/10.1080/09243046.2018.1433506>.
- [17] B. Budiansky, *Micromechanics*, *Comput. Struct.* 16 (1–4) (1983) 3–12, [http://dx.doi.org/10.1016/0045-7949\(83\)90141-4](http://dx.doi.org/10.1016/0045-7949(83)90141-4).
- [18] J.M. Fernandez, T.W. Murphey, A simple test method for large deformation bending of thin high strain composite flexures, in: 2018 AIAA Spacecraft Structures Conference, (January) AIAA, Kissimmee, FL, 2018, pp. 1–25, <http://dx.doi.org/10.2514/6.2018-0942>.
- [19] A.H. Sharma, T.J. Rose, A. Seamone, T.W. Murphey, F.L. Jiménez, Analysis of the column bending test for bending of high strain composites, in: AIAA Scitech 2019 Forum, (January) 2019, pp. 1–15, <http://dx.doi.org/10.2514/6.2019-1746>.
- [20] S.M. Oh, S.M. Lee, D.S. Kang, J.S. Roh, Microstructural changes of polyacrylonitrile-based carbon fibers (T300 and T700) due to isothermal oxidation (1): Focusing on morphological changes using scanning electron microscopy, *Carbon Lett.* 18 (1) (2016) 18–23, <http://dx.doi.org/10.5714/CL.2016.18.018>.
- [21] *NTPT Switzerland, NTPT Thinpreg402 - Datasheet, Tech. Rep.*, 2017.
- [22] F. Bosi, A. Schlothauer, S. Pellegrino, Cure-induced deformation of ultra-thin composite laminates, in: SciTech Forum 2018, (January) AIAA, Kissamee, FL, 2018, <http://dx.doi.org/10.2514/6.2018-2241>.
- [23] *I.M. Daniel, O. Lshai, Engineering Mechanics of Composite Materials, Oxford University Press, New York*, 1994.
- [24] R.D. Kriz, W. Stinchcomb, Elastic moduli of transversely isotropic graphite fibers and their composites, *Exp. Mech.* 19 (2) (1979) 41–49, <http://dx.doi.org/10.1007/BF02324524>.
- [25] M.J. Behr, B.G. Landes, B.E. Barton, M.T. Bernius, G.F. Billovits, E.J. Hukkanen, J.T. Patton, W. Wang, C. Wood, D.T. Keane, J.E. Rix, S.J. Weigand, Structure-property model for polyethylene-derived carbon fiber, *Carbon* 107 (2016) 525–535, <http://dx.doi.org/10.1016/j.carbon.2016.06.032>.
- [26] D.E. Soule, C.W. Nezbeda, Direct basal-plane shear in single-crystal graphite, *J. Appl. Phys.* 30 (11) (1968) 5122–5139, <http://dx.doi.org/10.1063/1.1655933>.
- [27] M.R. Wisnom, J.W. Atkinson, Constrained buckling tests show increasing compressive strain to failure with increasing strain gradient, *Composites A* 28 (11) (1997) 959–964, [http://dx.doi.org/10.1016/S1359-835X\(97\)00067-5](http://dx.doi.org/10.1016/S1359-835X(97)00067-5).
- [28] A. Schlothauer, N. Schwob, G.A. Pappas, P. Ermanni, Ultra-thin thermoplastic composites for foldable structures, in: AIAA Scitech 2020 Forum, (January) 2020, pp. 1–12, <http://dx.doi.org/10.2514/6.2020-0206>.